Electronic Supplementary Information (ESI)

Controllable Growth of Platinum Nanoparticles on Single-layer Transition-Metal Dichalcogenides for Size-Dependent Hydrogen Evolution Reaction Activities

Liang Mei,[a,‡] Xiaoping Gao,[b,‡] Zhao Gao,[c] Qingyong Zhang,[a] Xinge Yu,[c] Andrey L. Rogach,[a] Zhiyuan Zeng*,[a]

[a]*Department of Materials Science and Engineering, City University of Hong Kong, 83 Tat Chee Avenue, Kowloon, Hong Kong 999077, P. R. China*

[b]*School of Environmental Science and Engineering, Shanghai Jiao Tong University, 800 Dongchuan Road, Shanghai 200240, P. R. China*

[c]*Department of Biomedical Engineering, City University of Hong Kong, 83 Tat Chee Avenue, Kowloon, Hong Kong 999077, P. R. China*

[‡] These authors contributed equally to this work.

[*] Correspondence to: zhiyzeng@cityu.edu.hk (Z.Zeng)

Experimental Section

Chemicals

Molybdenum disulfide (MoS_2, 10-30 mm, Rose Mill), Tantalum disulfide (TaS_2, Alfa Aesar, Massachusetts, USA), Titanium disulfide (TiS_2, Sigma, Steinheim, Germany), N-methylpyrrolidone (NMP, Sigma), poly (vinylidene fluoride) (PVDF, Sigma), Lithium foil (ACME Research Support Pte Ltd), Lithium hexafluorophosphate ($LiPF_6$, Charslton Technologies Pte Ltd), Copper foil (ACME Research Support Pte Ltd), Polypropylene (pp) film (Celgard 2300), Sodium borohydride ($NaBH_4$, 99.99%, Sigma-Aldrich), Potassium tetrachloroplatinate (II) (K_2PtCl_4, 99.99% trace metals basis, Sigma-Aldrich), Tetradecyltrimethylammonium bromide ($C_{14}TABr$, 99 %, Sigma-Aldrich), Silicon oxide wafers were bought from Bonda Technology, Ethanol (>99.9%, Merck), acetone (Tech Grade, Aik Moh Paints & Chemicals Pte Ltd,) were

used as received. The Milli-Q water (Millipore, Billerica, MA) was used in all experiments.

Fabrication of single-layer TMDs nanosheets

Single-layer TMDs nanosheets were prepared by the previously reported electrochemical lithium intercalation method.[1] The intercalation process of cathode materials (bulk TMDs powder) was performed using the battery test systems by taking the Li foil as anode and 1M $LiPF_6$ as the electrolyte, which was dissolved in a mixture of ethyl carbonate (EC) and dimethyl carbonate (DMC) at a volume ratio of 1:1. The cathode material was prepared via mixing the layered bulk material (MoS_2, TaS_2 and TiS_2, respectively) with the acetylene black and PVDF (mass ratio = 8:1:1) dispersed in NMP solutions. Then, the resulting homogeneously slurry was uniformly coated on a copper foil and dried under vacuum at 100 ℃ for 24 hours. Battery was assembled in an Ar-filled glove box and galvanostatic discharge was conducted using the Neware battery test system to drive the lithium intercalation into the interlayer space of the bulk TMDs. After finishing the discharge process, the lithiated sample was washed with acetone to remove any residual $LiPF_6$, which was finally exfoliated in distilled water through the ultrasonication. The suspension was centrifuged to get the single-layer TMDs nanosheets.

Deposition of Pt NPs on single-layer TMDs nanosheets

1 ml of freshly prepared -single-layer TMDs nanosheets (MoS_2, TiS_2, TaS_2) was mixed with 13 ml aqueous solution containing 100 mM $C_{14}TABr$, 1 mM K_2PtCl_4, and Milli-Q water. The mixture was purged with N_2 gas for 15 min in order to remove the dissolved oxygen in solution. After that, the mixture was heated at 50 ℃ along with the stirring rate of 800 rpm, followed by adding 1 ml 420 mM $NaBH_4$. The whole process was conducted in N_2-saturated solution to avoid oxidation during Pt nanoparticles growth, and it can also release pressure resulting from the generated H_2 via vigorous reaction between excess $NaBH_4$ and water. During the reduction process, an obvious color change from light brown to dark yellowish brown was observed, indicating a

growth of Pt nanoparticles onto the TMDs nanosheets. After completing the reduction, the Pt-TMDs composites were collected via the centrifugation and washed with water for future characterization.

Characterization

A drop of diluted single-layer TMDs nanosheets or Pt decorated composites sample was coated onto an APTES-modified Si/SiO_2, holey carbon-coated copper grid, APTES-modified Si/SiO_2 and a silicon wafer respectively, and dried at room temperature in the fume hood before they were characterized by AFM (Dimension 3100 Veeco, CA), TEM (JEM-2100F), XPS (Axis Ultra) and SEM-EDX (JEOL-7600F).

Electrocatalytic measurements

MoS_2, Pt-MoS_2, and Pt-C were tested for the HER performance. The catalyst ink was prepared by mixing each sample with water, 99.9% ethanol and 5% Nafion perfluorinated resin solution (v/v/v= 4:1:0.1) respectively to form the electrode coating materials that containing 0.4 mg/ml of the catalyst (MoS_2 and Pt-MoS_2), while 0.196 mg/ml of Pt-C (commercial sample with 10 wt% Pt on activated charcoal) was also prepared in a similar manner to ensure a similar Pt loading (0.59 μg) on the electrode for Pt-MoS_2-1h and Pt-C samples, which then went through a 45 min ultrasonication to ensure ideal dispersion. Next, 3 μl well-dispersed electrode coating material was casted onto a glass carbon electrode (diameter of 3 mm). The coated glass carbon electrode was dried at room temperature, and then in a high vacuum environment at room temperature for 1-2 hours. The completely dried glass carbon electrode was tested in 0.5 M H_2SO_4 for its electrocatalytic properties using a typical three-electrode setup in room temperature, under nitrogen purged through the electrolyte to avoid the sample oxidation. Linear sweep voltammetry (LSV) was conducted at a scan rate of 0.002 V/s. CV was operated for 1000 cycles with a san rate of 0.1 V/s, followed by LSV to determine the cyclic stability. All the potentials were converted to values with reference to a reversible hydrogen electrode (RHE).

Density functional theory (DFT) calculations

All the spin-polarized density functional theory (DFT) calculations were carried out with the Dmol^3 code.[2] The exchange-correlation was described by the generalized gradient approximation (GGA) with the Perdew-Becke-Ernzerhof (PBE) function.[3, 4] The empirical correction in the Tkatchenko-Scheffler scheme was used to account for the long-range van der Waals (vdW) effects.[5] The DFT Semi-core Pseudopots and double numerical plus polarization (DNP) basis set were adopted for the transition-metal and sulfur atoms, respectively. The convergence threshold for the total energy, maximum force and displacement during the fully geometrical optimization were set to 10^{-5} Hartree, 0.002 Hartree/Å and 0.005 Å, respectively. For the structural optimization of the (4 × 4) supercell and the corresponding electronic structure calculations, the Brillioun zone were sampled by 5 × 5 × 1 and 9 × 9 × 1 Monkhorst-pack meshes, respectively. Electrostatic potential means the amount of work that moves a unit of charge from a reference point (such as at infinity) to a specific point inside the field. Low electrostatic potential denotes weak adsorption energy of the H atom on active sites in this study. Density of states (DOS) of a system describes the proportion of states that are to be occupied by the system at each energy. High DOS at a specific energy level means that many states are available for occupation. A vacuum of 20 Å in the *z*-direction in periodically boxes was used to avoid the interactions between periodic images. To consider the water solvent effects, the conductor-like screening model (COSMO) with the dielectric constant of 78.54 was used during all the calculations.[6]

The adsorption energies (ΔE_{ads}) are calculated via the following expression (1):

$$\Delta E_{ads} = E_{substrate + adsorbent} - E_{substrate} - E_{adsorbent} \quad (1)$$

where the $E_{substrate + adsorbent}$, $E_{substrate}$, and $E_{adsorbent}$ refer to the total energies of the substrate with adsorbent composites, the substrate, and the adsorbent, respectively. The more negative value of ΔE_{ads} illustrates the stronger binding between intermediate and catalyst as well as the better thermodynamic stability.

There are two steps for HER to generate H_2: a) the atomic H adsorption on the surface of catalysts, b) the formation and release of H_2.[7] The HER performance can be evaluated through ΔG_{H^*}:

$$H^+ + e^- + * \xrightarrow{\Delta G_{H^*}} H^* \quad (2)$$

where H* and * are the adsorbed hydrogen intermediate and the active site on the catalyst, respectively. Under the standard conditions (pH=0, U=0, and 298.15 K), the free energy of $H^+ + e^-$ ($\mu_{(H^+ + e^-)}$) is equivalent to that of $1/2H_2$. Therefore, the ΔG_{H^*} is calculated by:

$$\Delta G_{H^*} = \Delta E_{H^*} + \Delta E_{ZPE} - T\Delta S_{H^*} \quad (3)$$

where ΔE_{H^*} is the energy of hydrogen adsorption obtained from equation (1). The hydrogen intermediate state (H*) in the HER was tested with several different initial configurations on the electrocatalysts, and the following calculated results analysis are based on the most stable structures. ΔE_{ZPE} is the zero-point energy difference between gas-phase H_2 and the adsorbed H obtained by the equation $\Delta E_{ZPE} = E_{ZPE}^{H*} - E_{ZPE}^{*} - 1/2E_{ZPE}^{H2}$, where E_{ZPE}^{*}, E_{ZPE}^{H*}, and E_{ZPE}^{H2} are the zero-point energies of pure substrate, an adsorbed hydrogen on the substrate, and gas phase H_2, respectively. T is the temperature at 298K. The value of ΔS_{H^*} can be described as $1/2\, S_{H2}^{0}$ because of the calculated small vibrational entropy of the adsorbed state H*, where S_{H2}^{0} refers to the entropy of gas phase H_2 and is about 130 $J \cdot mol^{-1} \cdot K^{-1}$ at the standard conditions.[8] The ideal ΔG_{H^*} value for HER is zero, and too strong or too weak binding energy of the intermediate state would lead to low HER performance.

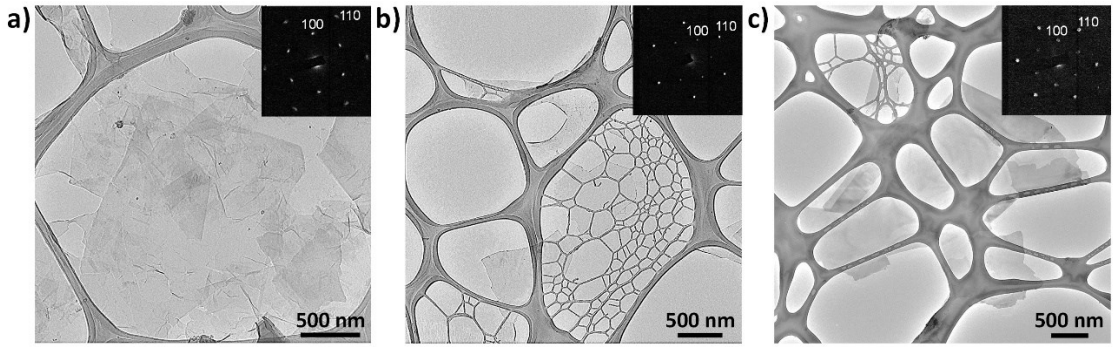

Fig. S1 TEM images of single-layer a) MoS_2 nanosheets, b) TiS_2 nanosheets, and c) TaS_2 nanosheets, with insets providing their SAED patterns.

TEM images of MoS_2, TiS_2 and TaS_2 nanosheets in Fig. S1 show that their contrast is very weak, since these are single-layers. The corresponding selected area electron diffraction (SAED) pattern of a flat area of the nanosheets shows the hexagonal lattice structure with (100) and (110) planes indexed, respectively.

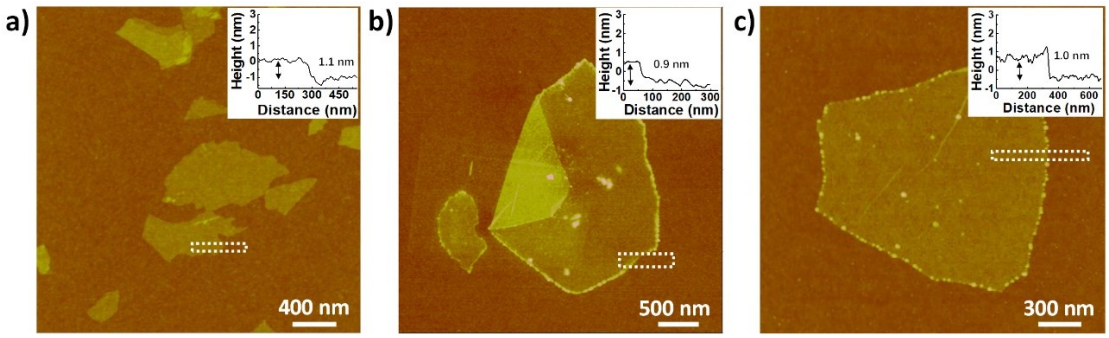

Fig. S2 AFM images of a) MoS_2, b) TiS_2 and c) TaS_2 nanosheets, deposited on Si/SiO_2 substrates. The line height scans over the AFM images shown in insets provide the thickness estimation of ~1.0 nm, which confirms that single-layer MoS_2, TiS_2 and TaS_2 nanosheets were successfully produced.

AFM images of MoS_2, TiS_2 and TaS_2 nanosheets in Fig. S2 reveal their thickness of around 1.0 nm, which further confirmed that single-layer MoS_2, TiS_2 and TaS_2 nanosheets were successfully prepared.

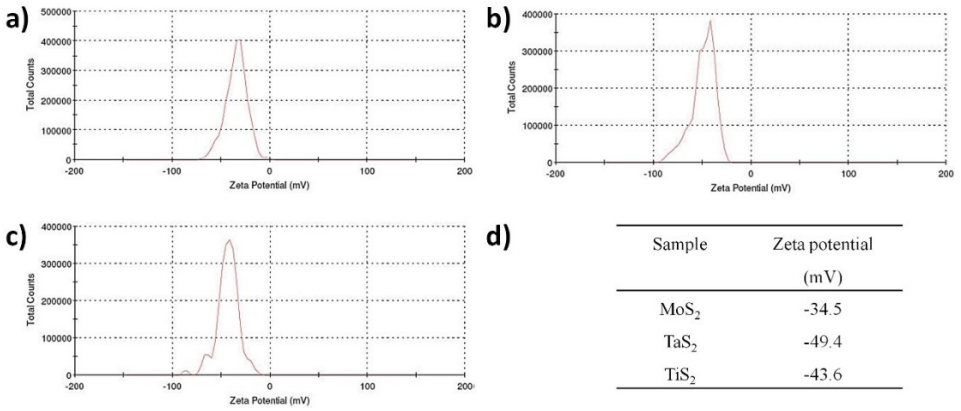

Sample	Zeta potential (mV)
MoS_2	-34.5
TaS_2	-49.4
TiS_2	-43.6

Fig. S3 Zeta potential scans of single-layer a) MoS_2, b) TaS_2 and c) TiS_2 dispersions. d) Corresponding Zeta potential values for the three dispersions.

Zeta potential is the most important indicator of stability of colloidal dispersions, as it provides an extent of electrostatic repulsion between adjacent charged particles in a dispersion. Hence, we performed zeta potential measurements to evaluate the stability of the fabricated single-layer TMD nanosheets dispersion, as shown in Fig. S3. Zeta potentials of MoS_2, TaS_2 and TiS_2 nanosheets were -34.5 mV, -49.4 mV and -43.6 mV, respectively, and thus in the range of moderate to good stability.[9] High negative surface charge of these single-layer TMD dispersions guarantee their long-term stability via repulsive force between each other to prevent the aggregation by the Van der Waals forces.

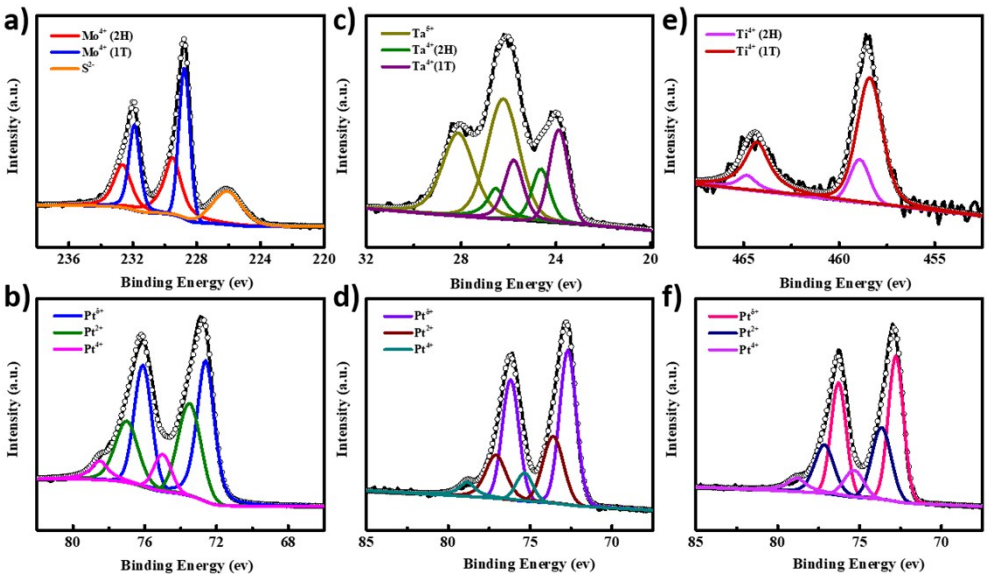

Fig. S4 XPS a) Mo 3d spectra and b) Pt 4f spectra of Pt-MoS_2-1h composites. c) Ta 4f spectra and d) Pt 4f spectra of Pt-TaS_2-1h composites. e) Ti 2p spectra and f) Pt 4f spectra of Pt-TiS_2-1h composites.

In Fig. S4a, c, e, both 1T and 2H phases do exist in the exfoliated TMDs nanosheets prepared via the lithium intercalation and exfoliation method, which is in agreement with previous literature.[10] In addition, impurities of Ta^{5+} were also present in the Pt-TaS_2 nanosheets. For the Pt NP characterization, as shown in Fig. S4b, d, f, no peaks of Pt^0 were detected but the bands of the $Pt^{\delta+}$ were present, which is due to the substrate-catalyst interaction, that is, the electron transfer from the Pt NPs to the TMDs

nanosheets.[10, 11] This means that 2D TMD nanosheets hold the advantages of large exposed surface area, which facilitates efficient charge transfer and ionic exchange at the surface of catalyst.

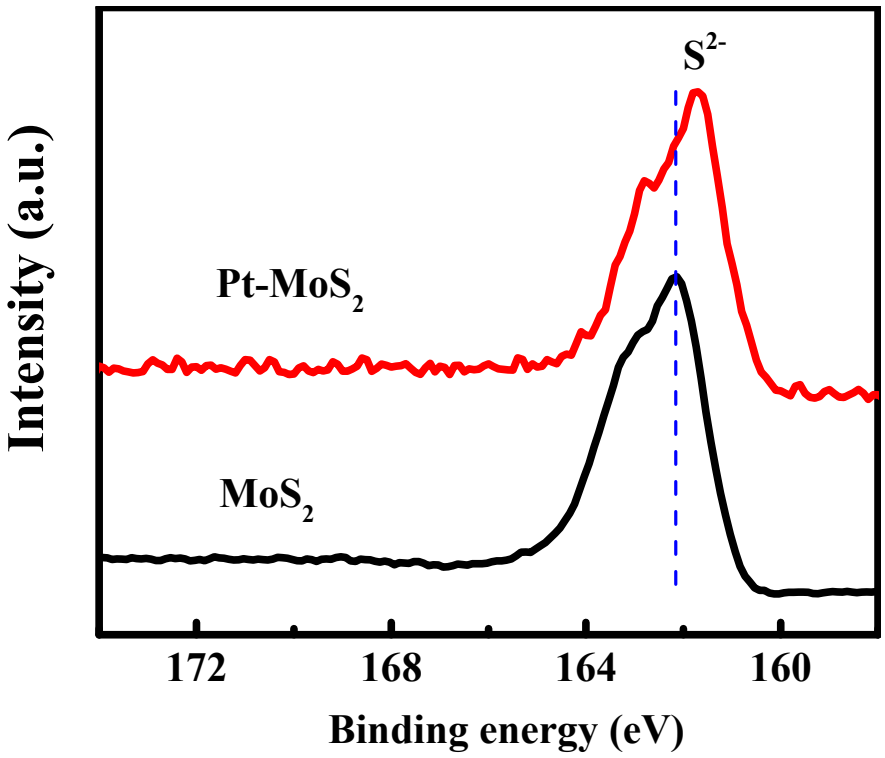

Fig. S5 XPS of S2p spectra of as-prepared MoS_2 nanosheets and Pt-MoS_2 nanocomposites.

From Fig. S5, after decorating the Pt NPs on MoS_2 nanosheets, the binding energies of the S2p bands shifted to the lower value, this is attributed to the electrons transfer from Pt to S,[12] that's why no peak of Pt^{0+} was detected in Pt-MoS_2 composites.

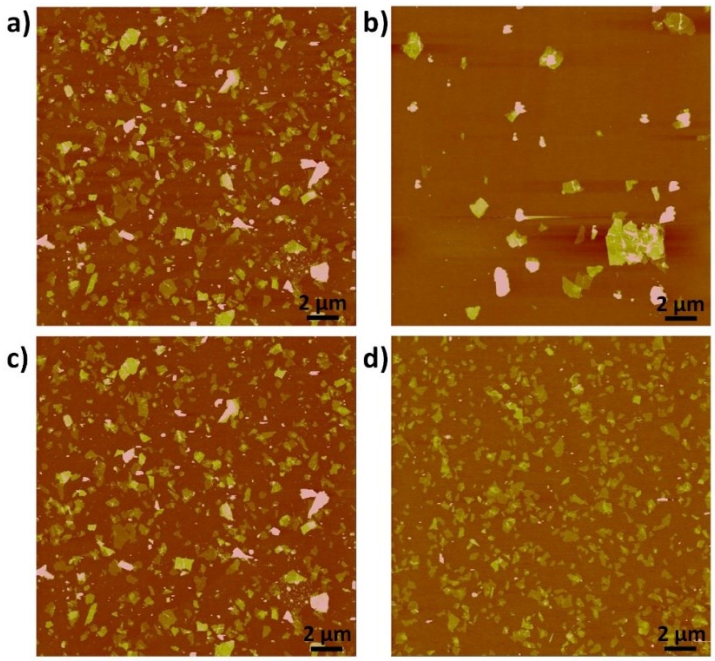

Fig. S6 AFM images of large-area MoS_2 nanosheets deposited on Si/SiO_2 substrates using two-step centrifugation procedure under different rotational speed and time to explore the optimal synthesis conditions. a) 0 - 10000 rpm, 15 min. b) 1000 rpm, 30 min - 3000 rpm, 15 min. c) 3000 rpm, 15 min - 10000 rpm, 15 min. d) 3000 rpm, 30 min - 10000 rpm, 15 min.

Centrifugation is a universal and effective method to purify and optimize the quality of the prepared nanomaterials, which we have applied in this work to separate the single-layer TMDs nanosheets from the unexfoliated bulk materials as well as from the carbon NPs (acetylene black) in solution. In order to obtain monodisperse single-layer TMDs nanosheets with high purity as well as uniform lateral size for Pt NPs deposition, we adopted several control experiments using two-step centrifugation procedure under different rotational speed and time to explore the optimal synthesis conditions. AFM images of large amount of MoS_2 nanosheets deposited on Si/SiO_2 substrates (Fig. S6) shows that under two-step centrifugation condition (Sorvall Legend Micro 21 microcentrifuge) with a first centrifugation step "3000 rpm, 30 min" and a second centrifugation step "10000 rpm, 15 min", a dispersion of single-layer MoS_2 nanosheets with sheets' lateral size of around 0.6 - 1 µm was obtained. Importantly, as observed from the AFM images, there were no particle-like or multilayer by-products in this

dispersion, which guarantees high quality Pt-MoS_2 composite fabrication using such single-layer MoS_2 nanosheets with rather uniform lateral size distribution as the template.

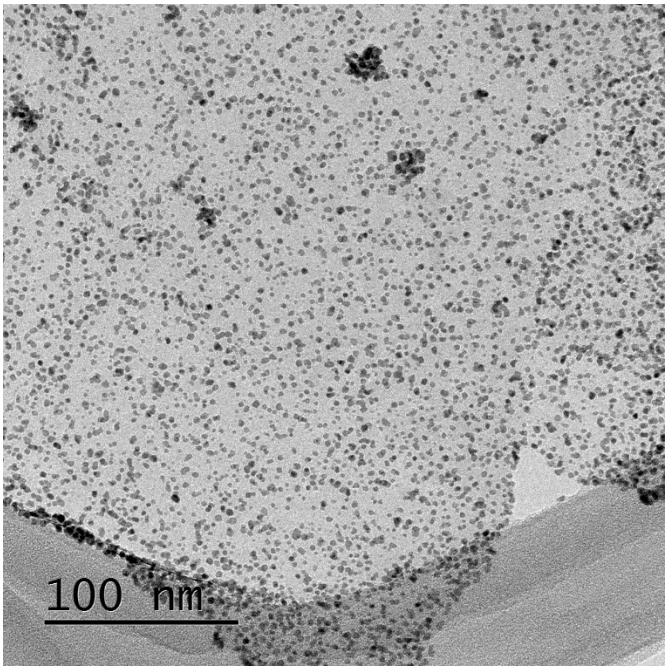

Fig. S7 High resolution TEM image of Pt-MoS_2-0.5h.

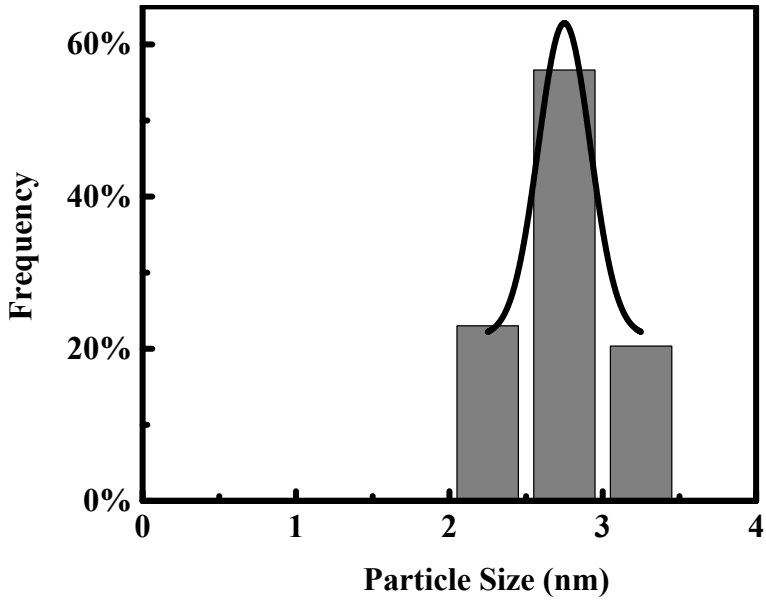

Fig. S8 The Pt nanoparticle size distribution of Pt-MoS_2-0.5h and the Gauss fit. The size distribution analysis was performed by counting over 100 Pt NPs in Fig. S7 using ImageJ software.

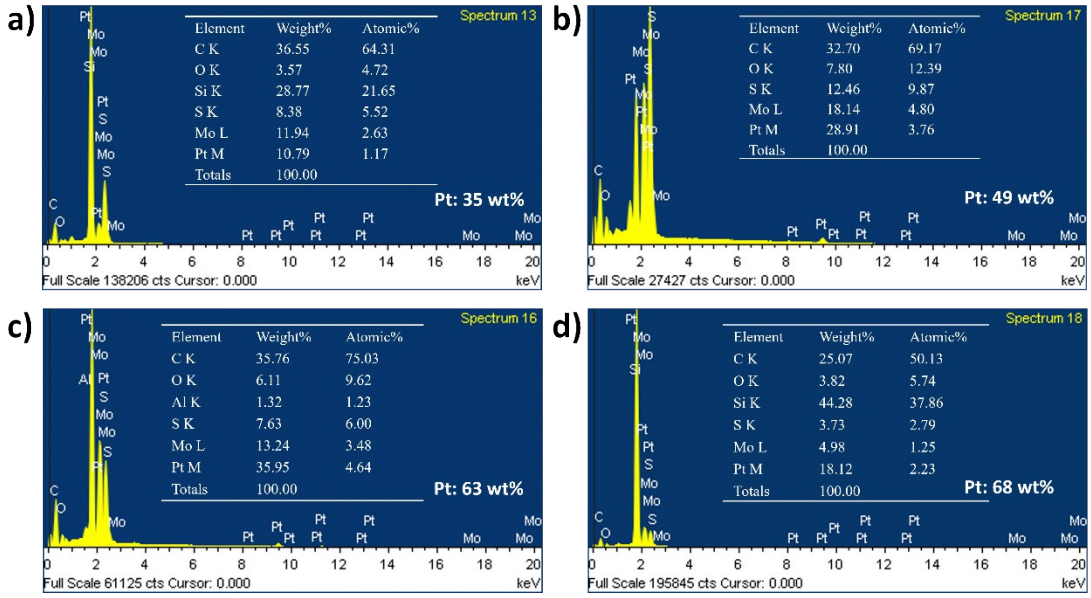

Fig. S9 EDS analysis of a) Pt-MoS_2- 0.5h, b) Pt-MoS_2- 1h, c) Pt-MoS_2- 2h, d) Pt-MoS_2- 4h composites deposited on Si/SiO_2 substrates. The Pt contents in the four composites are 35 wt%, 49 wt%, 63 wt%, 68 wt%, respectively.

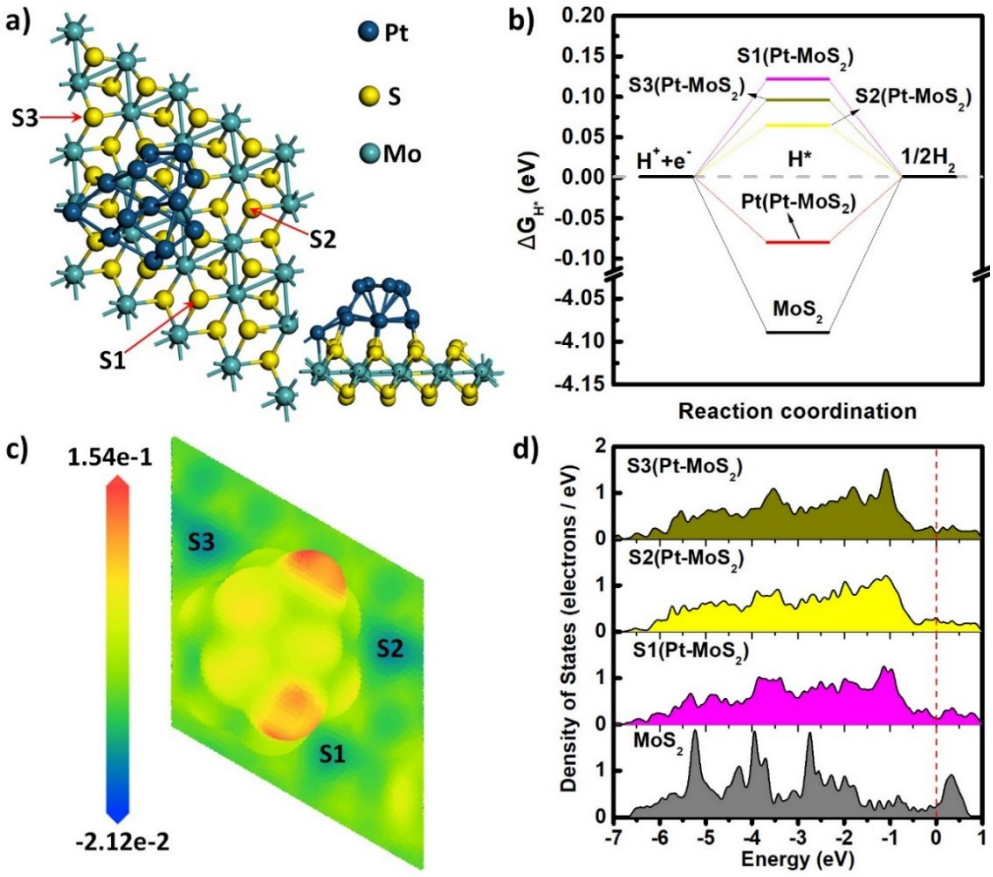

Fig. S10 a) Top and side views of the optimized Pt_{13}-MoS_2 structures. b) Gibbs free energy for H* adsorption on in-plane S site of the pristine 1T-MoS_2 and on the Pt and in-plane S sites of Pt_{13}-MoS_2. c) Electrostatic potential map of the Pt_{13}-MoS_2 electrocatalyst. d) DOS of the in-plane S sites of the pristine 1T-MoS_2 and Pt_{13}-MoS_2 electrocatalyst. The red dashed line indicates the Fermi level.

The Gibbs free energy for H* adsorption (ΔG_{H^*}) on the active sites of electrocatalysts is a crucial descriptor for their HER performance. The closer ΔG_{H^*} is to 0 eV, the better is the HER activity of the electrocatalyst.[13] We considered Pt_{13} cluster, the smallest magic cluster according to the geometric shell model,[14] placed on a 1T-MoS_2 nanosheet, which we name Pt_{13}-MoS_2 composite (Fig. S10a), as a model to theoretically investigate the synergy in HER between Pt and MoS_2. The ΔG_{H^*} values of Pt-MoS_2 on all possible active sites were calculated (see calculation details in experimental section) and are presented in Fig. S10b. ΔG_{H^*} of the in-plane S site of pure 1T-MoS_2 was calculated, as well. The adsorption of H* on the in-plane S sites of pure 1T-MoS_2 is strong, with ΔG_{H^*} equal to -4.09 eV. Placing Pt_{13} on 1T-MoS_2 not only results in an excellent HER activity of Pt with ΔG_{H^*} equal to -0.08 eV (Fig. S10b), which is quite close to the value (-0.09 eV) that reported by the literature,[7] but also contributes to the decrease of the absolute values $|\Delta G_H^*|$ for the S1, S2, and S3 sites of MoS_2 from 4.09 eV to 0.12, 0.06 and 0.10 eV, respectively, which means the adsorption strength of H* on the S atoms around the Pt_{13} is weakened. (Fig. S10b). The high HER activity of the activated S sites greatly enhances the catalytic performance of the Pt-MoS_2 electrocatalyst. This confirms the synergy effect between Pt NPs and the in-plane S sites of MoS_2, which is in line with our experimental results (Fig. 4a). Considering the high coverage of H* on the Pt NPs under negative potential, the binding strength of H* on the Pt sites will be weakened, thus the HER activity of Pt sites will increase.[15] Furthermore, electronic properties of the Pt-MoS_2 electrocatalyst were also computed (see calculation details in experimental section) to gain the insights into the variation of HER activity. The electrostatic potential map of the Pt_{13}-MoS_2 catalyst shows that S1, S2, and S3 sites have lower electrostatic potential than that of the other in-plane S

sites (Fig. S10c), which indicates the activation of the S1, S2, and S3 sites. In addition, density of states (DOS) of the S1, S2, and S3 sites of Pt_{13}-MoS_2 displays disappearance of electronic state near the Fermi level in comparison with that of pristine MoS_2 (Fig. S10d), being able to reduce the hybridization between H* and the sulfur atoms, and thus to weaken the corresponding H* adsorption.

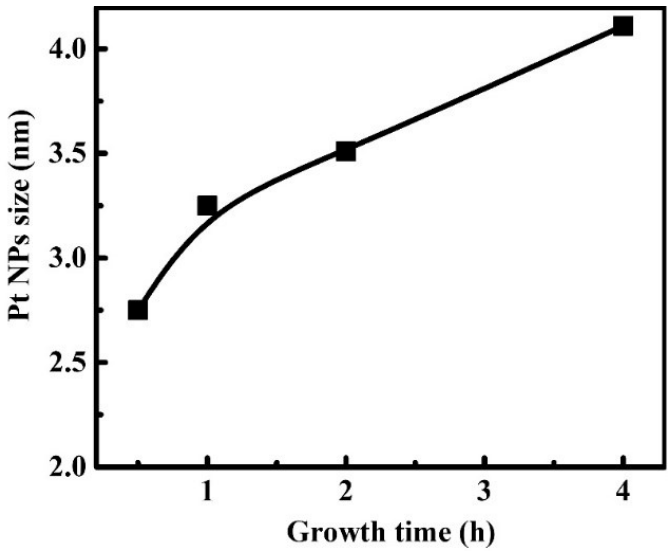

Fig. S11 Change of Pt NP size with growth time.

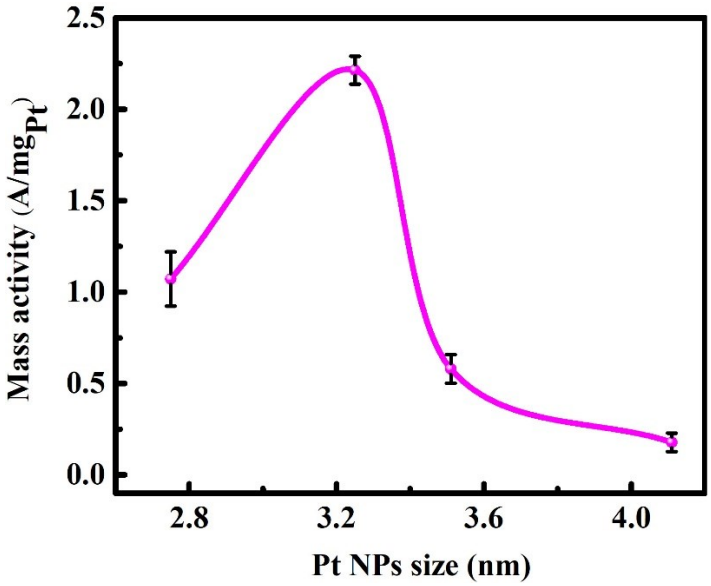

Fig. S12 Mass activity of Pt-MoS_2 composites as a function of average Pt NP size at overpotential of 120 mV (vs. RHE). Error bars indicate the standard deviations from three different experiments.

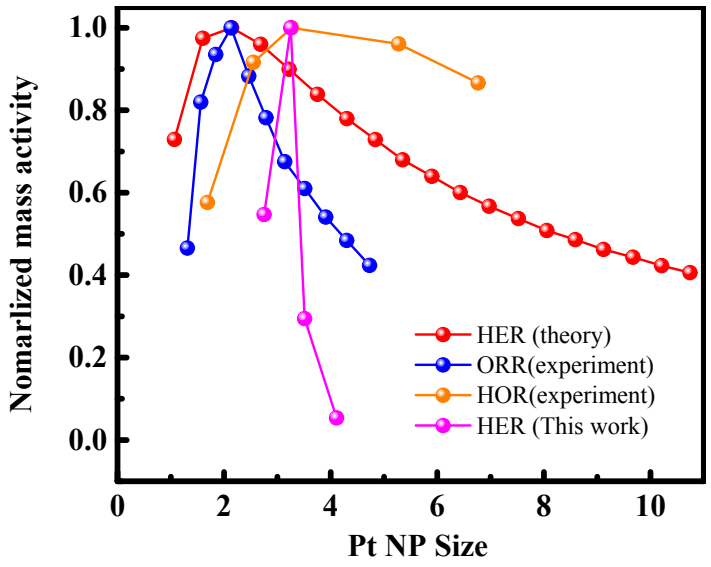

Fig. S13 Overview the literature reported normalized Pt mass activity as a function of Pt NP size for different electrocatalytic reactions.

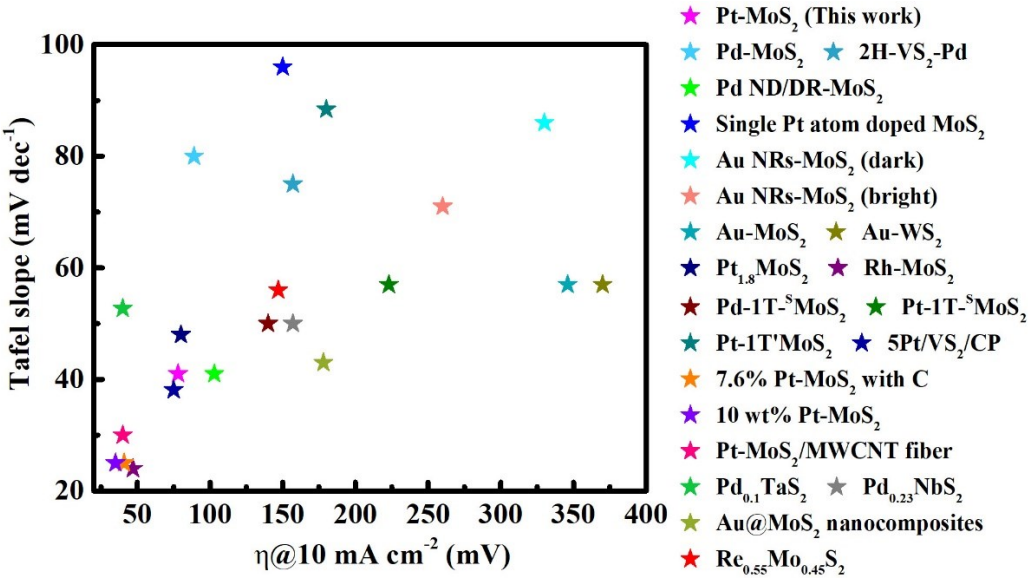

Fig. S14 Comparison of the overpotentials (η) at 10 mA cm^{-2} and the Tafel slopes between previously reported precious metal-TMDs composites and the Pt-MoS_2-1h composite obtained in this work (magenta star).

Table S1. Summary of electrocatalytic performance of the materials studied in this work.

Material	Onset potential	Tafel slope	Exchange current

	(mV vs RHE)	(mV/dec)	density (μA/cm^2)
MoS_2	204	92	0.43
Pt-MoS_2- 0.5hr	3	49	178.89
Pt-MoS_2- 1hr	~0	41	337.53
Pt-MoS_2- 2hr	8	56	144.68
Pt-MoS_2- 4hr	55	72	27.97
Pt-C	~0	30	744.70

Exchange current density is another indicator for the electrocatalytic performance, which can be calculated applying the extrapolation method to the Tafel plot. As shown in Table S1, the exchange current density increased from 0.43 μA/cm^2 (MoS_2) to 337.53 μA/cm^2 (Pt-MoS_2-1h), which is an improvement by 785 times. Three other Pt-MoS_2 catalysts also showed enhanced exchange current density as compared with pristine MoS_2 (178.89, 144.68 and 27.97 μA/cm^2 for Pt-MoS_2-0.5h, Pt-MoS_2-2h and Pt-MoS_2-4h, respectively), which means that the Pt-MoS_2 composites are much easier to polarize than the blank MoS_2, which facilitates the improved hydrogen production under the lower overpotential.

Table S2. Comparison of the electrocatalytic activity of Pt-MoS_2-1h composite obtained in this work with some previously reported precious metal decorated TMDs materials for HER application in 0.5M H_2SO_4.

Electrocatalyst	Onset potential (mV vs RHE)	Overpotential @ 10mA/cm^2 (mV vs RHE)	Tafel slope (mV/dec)	Exchange current Density (μA/cm^2)
Pt-MoS_2-1h (this work)	~0	78.5	41	337.5
Pt-MoS_2[16]	9	-	44	373
Pt-TiS_2[17]	-	-	40.6	-
Pt-TaS_2[17]	-	-	54	-
Pt/MoS_2[18]	31	-	52	256
$Pt_{1.8}MoS_2$[19]	-	80	48	-

Pt-1T'MoS_2[20]	-	180	88.4	-
5Pt/VS_2/CP[21]	-	75	38.1	-
7.6% Pt−MoS_2 with C[22]	~0	41	25	-
10 wt%Pt-MoS_2[23]	~22	~35	~25	-
Pt-MoS_2/MWCNT fiber[24]	-	40	30	455.4
Pd-MoS_2[25]	-	89	80	805
Pd ND/DR-MoS_2[26]	40	103	41	426.6
$Pd_{0.1}TaS_2$[27]	77	121	52.7	-
$Pd_{0.23}NbS_2$[28]	99	157	50	-
2H-VS_2-Pd[29]	-	157	75	-
Single Pt atom doped MoS_2[30]	-	150	96	-
Au NRs-MoS_2[31] (dark)	220	330	86	-
Au NRs-MoS_2[31] (bright)	160	260	71	-
Au-MoS_2[32]	205	346	57	-
Au-WS_2[32]	230	370	57	-
Au@MoS_2 nanocomposite[33]	-	178	43	-
Pd-1T-$^{S}MoS_2$[34]	-	140	50	-
Pt-1T-$^{S}MoS_2$[34]	-	223	57	-
1T MoS_2−Au/Pd[35] (dark)	50	-	63	-
1T MoS_2−Au/Pd[35] (light)	~0	-	49	-
Rh-MoS_2[36]	-	47	24	8.8
$Re_{0.55}Mo_{0.45}S_2$[37]	90	147	56	27

Reference

1 Z. Y. Zeng, Z. Y. Yin, X. Huang, H. Li, Q. Y. He, G. Lu, F. Boey and H. Zhang, *Angew. Chem. Int. Ed.*, 2011, **50**, 11093-11097.

2 B. Delley, *J. Chem. Phys.*, 2000, **113**, 7756-7764.

3 J. P. Perdew, K. Burke and M. Ernzerhof, *Phys. Rev. Lett*, 1996, **77**, 3865-3868.

4 J. P. Perdew, J. A. Chevary, S. H. Vosko, K. A. Jackson, M. R. Pederson, D. J. Singh and C. Fiolhais, *Phys. Rev. B*, 1993, **48**, 4978-4978.

5 S. Grimme, *J. Comput. Chem*, 2006, **27**, 1787-1799.

6 A. Klamt and G. Schuurmann, *J. Chem. Soc.-Perkin Transactions 2*, 1993, DOI:

10.1039/p29930000799, 799-805.
7 J. K. Norskov, T. Bligaard, A. Logadottir, J. R. Kitchin, J. G. Chen, S. Pandelov and J. K. Norskov, *J. Electrochem. Soc*, 2005, **152**, J23-J26.
8 Q. Tang and D. E. Jiang, *ACS Catal.*, 2016, **6**, 4953-4961.
9 N. S. Souza, A. D. Rodrigues, C. A. Cardoso, H. Pardo, R. Faccio, A. W. Mombru, J. C. Galzerani, O. F. de Lima, S. Sergeenkov and F. M. Araujo-Moreira, *Phys. Lett. A*, 2012, **376**, 544-546.
10 X. Huang, Z. Y. Zeng, S. Y. Bao, M. F. Wang, X. Y. Qi, Z. X. Fan and H. Zhang, *Nat. Commun.*, 2013, **4**, 1444.
11 F. Sen and G. Gokagac, *J. Phys. Chem. C*, 2007, **111**, 5715-5720.
12 Y. P. Luo, D. K. Huang, M. Li, X. Xiao, W. N. Shi, M. K. Wang, J. Su and Y. Shen, *Electrochim. Acta*, 2016, **219**, 187-193.
13 J. K. Nørskov, T. Bligaard, A. Logadottir, J. R. Kitchin, J. G. Chen, S. Pandelov and U. Stimming, *J. Electrochem. Soc.*, 2005, **152**, J23.
14 I. A. Solov'yov, A. V. Solov'yov, W. Greiner, A. Koshelev and A. Shutovich, *Phys. Rev. Lett.*, 2003, **90**, 053401.
15 T. T. Yang, T. L. Tan and W. A. Saidi, *Chem. Mater.*, 2020, **32**, 1315-1321.
16 S. Li, J. K. Lee, S. Zhou, M. Pasta and J. H. Warner, *Chem. Mater.*, 2019, **31**, 387-397.
17 Z. Y. Zeng, C. L. Tan, X. Huang, S. Y. Bao and H. Zhang, *Energy Environ. Sci.*, 2014, **7**, 797-803.
18 W. N. Ren, H. F. Zhang and C. W. Cheng, *Electrochim. Acta*, 2017, **241**, 316-322.
19 X. Y. Chia, N. A. A. Sutrisnoh and M. Pumera, *ACS Appl. Mater. Interfaces*, 2018, **10**, 8702-8711.
20 C. Q. Wu, D. D. Li, S. Q. Ding, Z. U. Rehman, Q. Liu, S. M. Chen, B. Zhang and L. Song, *J. Phys. Chem. Lett.*, 2019, **10**, 6081-6087.
21 J. T. Zhu, L. J. Cai, X. M. Yin, Z. Wang, L. F. Zhang, H. B. Ma, Y. X. Ke, Y. H. Du, S. B. Xi, A. T. S. Wee, Y. Chai and W. J. Zhang, *ACS Nano*, 2020, **14**, 5600-5608.
22 P. Zuo, L. Jiang, X. Li, B. Li, P. Ran, X. J. Li, L. T. Qu and Y. F. Lu, *ACS Sustain. Chem. Eng.*, 2018, **6**, 7704-7714.
23 Z. X. Chen, K. Leng, X. X. Zhao, S. Malkhandi, W. Tang, B. B. Tian, L. Dong, L. R. Zheng, M. Lin, B. S. Yeo and K. P. Loh, *Nat. Commun.*, 2017, **8**, 14548.
24 B. Chen, G. Z. Sun, J. Wang, G. G. Liu, C. L. Tan, Y. Chen, H. F. Cheng, J. Z. Chen, Q. L. Ma, L. Huang, P. Chen and H. Zhang, *Chem. Commun.*, 2020, **56**, 5131-5134.
25 Z. Y. Luo, Y. X. Ouyang, H. Zhang, M. L. Xiao, J. J. Ge, Z. Jiang, J. L. Wang, D. M. Tang, X. Z. Cao, C. P. Liu and W. Xing, *Nat. Commun.*, 2018, **9**, 2120.
26 K. Qi, S. S. Yu, Q. Y. Wang, W. Zhang, J. C. Fan, W. T. Zheng and X. Q. Cui, *J. Mater. Chem. A*, 2016, **4**, 4025-4031.
27 D. Wang, X. Wang, Y. Lu, C. S. Song, J. Pan, C. L. Li, M. L. Sui, W. Zhao and F. Q. Huang, *J. Mater. Chem. A*, 2017, **5**, 22618-22624.
28 C. Huang, X. Wan, D. Wang, W. Zhao, K. J. Bu, J. J. Xu, X. Y. Huang, Q. Y. Bi, J. Huang and F. Q. Huang, *Chem. Mater.*, 2019, **31**, 4726-4731.
29 K. Karthick, T. K. Bijoy, A. Sivakumaran, A. B. M. Basha, P. Murugan and S. Kundu, *Inorg. Chem.*, 2020, **59**, 10197-10207.
30 J. Deng, H. B. Li, J. P. Xiao, Y. C. Tu, D. H. Deng, H. X. Yang, H. F. Tian, J. Q. Li, P. J. Ren and X. H. Bao, *Energy Environ. Sci.*, 2015, **8**, 1594-1601.
31 Y. Shi, J. Wang, C. Wang, T. T. Zhai, W. J. Bao, J. J. Xu, X. H. Xia and H. Y. Chen, *J. Am. Chem. Soc.*, 2015, **137**, 7365-7370.

32 J. Kim, S. Byun, A. J. Smith, J. Yu and J. X. Huang, *J. Phys. Chem. Lett.*, 2013, **4**, 1227-1232.

33 Z. Q. Liu, X. Zhang, Y. Gong, Q. P. Lu, Z. C. Zhang, H. F. Cheng, Q. L. Ma, J. Z. Chen, M. T. Zhao, B. Chen, Y. Chen, X. J. Wu, P. F. Yin, L. Gu, Y. P. Du and H. Zhang, *Nano Res.*, 2019, **12**, 1301-1305.

34 T. H. M. Lau, S. Wu, R. Kato, T. S. Wu, J. Kulhavy, J. Y. Mo, J. W. Zheng, J. S. Foord, Y. L. Soo, K. Suenaga, M. T. Darby and S. C. E. Tsang, *ACS Catal.*, 2019, **9**, 7527-7534.

35 B. Shang, X. Q. Cui, L. Jiao, K. Qi, Y. W. Wang, J. C. Fan, Y. Y. Yue, H. Y. Wang, Q. L. Bao, X. F. Fan, S. T. Wei, W. Song, Z. L. Cheng, S. J. Guo and W. T. Zheng, *Nano Lett.*, 2019, **19**, 2758-2764.

36 Y. F. Cheng, S. K. Lu, F. Liao, L. B. Liu, Y. Q. Li and M. W. Shao, *Adv. Funct. Mater.*, 2017, **27**, 1700359.

37 S. Z. Yang, Y. J. Gong, P. Manchanda, Y. Y. Zhang, G. L. Ye, S. M. Chen, L. Song, S. T. Pantelides, P. M. Ajayan, M. F. Chisholm and W. Zhou, *Adv. Mater.*, 2018, **30**, 1803477.